Optimal Planning of Standalone Net-Zero Energy Systems with Small Modular Reactors

Mingyu Huang, *Student Member, IEEE,* Xueyuan Cui, *Student Member, IEEE,* Ning Zhang, *Member, IEEE,* Mengshuo Jia, *Member, IEEE,* and Yi Wang *Member, IEEE,*

***Abstract*—Renewable-based standalone systems are widely developed worldwide with the decentralization of power and energy systems. However, challenges are posed due to the intermittent nature of renewable resources and the lack of inertia. Small modular reactors (SMRs), a clean but also flexible and controllable energy, can be deployed to provide flexibility and inertia support to standalone energy systems with high penetration of renewable energy. In this paper, we propose a novel standalone net-zero energy system planning scheme that coordinates SMRs with other distributed energy resources, where both steady-state operation constraints and dynamic frequency security constraints are considered to guarantee the operational feasibility of the plan. Since the dynamics of SMR are very complex, the planning model becomes a complex and unanalytical optimization problem. To this end, we first develop a physics-informed data-driven approach to model the dynamic frequency characteristics of SMRs with high accuracy. On this basis, we propose a "checking and adjusting" heuristic approach to iteratively solve a series of MILP problems without the non-linear and unanalytical frequency constraint and then check whether the constraint can be satisfied. In this way, we can get a feasible and suboptimal solution in a tractable manner. Comprehensive case studies have been conducted, and results show that the inclusion of SMRs can substantially increase the flexibility and frequency security of standalone net-zero energy systems.**

***Index Terms*—Small modular reactor, net-zero energy system, optimal planning, frequency security constraints**

I. Introduction

STANDALONE energy systems, also known as off-grid energy systems, have emerged as a critical solution for providing electricity in areas far from the utility grid. These systems have been deployed for a wide range of applications worldwide, including remote communities, industrial facilities, mining operations, etc. As a significant part of the power and energy system, standalone energy systems have become even more important in the transition to net-zero emissions [1]. In net-zero transition, integrating a high penetration of renewable energy is an inevitable development trend [2]. However, renewable energy integration will bring two challenges that should be carefully considered when designing a net-zero standalone energy system: 1) the availability of renewable energy resources varies significantly with weather and seasons, which challenges the supply-demand balance [3]; 2) renewable energy resources are connected to the system through power electronics devices with no rotating inertia, which challenges the frequency security [4]. Therefore, there remains a need for clean and controllable sources to promote the net-zero development of standalone energy systems.

The most common solution is to incorporate renewable energy resources with a sizeable energy storage system, thereby helping to meet the supply-demand balance [5]. However, large energy storage systems can be relatively expensive. Furthermore, energy storage systems could not tackle the lack of inertia. In this case, additional clean energy resources with inertia support are needed. A potential option is to use solar thermal energy [6], which is dispatchable and involves a synchronous generator providing the necessary inertia to help maintain frequency security. Unfortunately, the sites of solar thermal plants are strictly restricted (usually in the desert) [7].

Small modular reactors (SMRs), an emerging and promising nuclear technology, can be deployed to provide both flexibility and inertia support [3]. The technical and economic characteristics of SMR have been reported by the International Atomic Energy Agency (IAEA) [8]. The dynamic process of SMR is consistent with large-scale nuclear power plants since they follow the same physical principles and operation modes, including pressurized water reactors, gas-cooled reactors, liquid metal reactors, etc. The differences between SMRs and classical large-scale nuclear power plants lie in the following three aspects [3]. 1) Modular design with a small generation scale, which allows for standardization, factory-based manufacturing, and simplified on-site installation. 2) Flexibility in power output. Unlike classical nuclear power plants, which typically operate at or near rated power levels, SMRs could adjust their power output flexibly. 3) Secure operation and transportation environment. SMRs are designed as sealed and transportable units, which reduces operational complexity, particularly for deployments at remote sites. The power management options of SMRs are threefold: multi-modular operation, reactor power maneuvering, and steam valve bypassing, which could be utilized for supply-demand balance in different time frames. In addition, the rotating inertia and frequency regulation support from SMR can help sustain frequency security. The design targets of SMRs include the power supply for remote areas, district heating, and industrial applications. Although most SMRs are still under

The work was supported in part by the National Key R&D Program of China (2022YFB2403300), and in part by the Research Grants Council of the Hong Kong SAR (HKU 27203723). (*Corresponding author: Mengshuo Jia.*)

Mingyu Huang, Xueyuan Cui, and Yi Wang are with the Department of Electrical and Electronic Engineering, The University of Hong Kong, Hong Kong SAR, China, and are also with The University of Hong Kong Shenzhen Institute of Research and Innovation, Shenzhen, 518057, China (e-mail: myhuang@eee.hku.hk, xycui@eee.hku.hk, yiwang@eee.hku.hk).

Ning Zhang is with the State Key Lab of Power Systems, Department of Electrical Engineering, Tsinghua University, Beijing 100084, China (e-mail: ningzhang@tsinghua.edu.cn).

Mengshuo Jia is with the Power Systems Laboratory, ETH Zürich, 8092 Zürich, Switzerland (jia@eeh.ee.ethz.ch).

design or construction, there are technical projects proposed for the SMR-integrated net-zero microgrids [9], [10], [11]. For example, the potential utilization of SMRs in Canada has been analyzed with detailed roadmaps [12].

In the literature, the integration of SMRs into the energy system has been investigated from different perspectives. In terms of modeling, the detailed dynamic process of the reactor was analyzed and integrated with the turbine-governor system in [13], with which the contribution of SMR dynamics in power system frequency response was evaluated. In terms of control, feedback controllers for reactor power adjustment were designed to ensure the system frequency was well-regulated during load disturbances [14]. In terms of scheduling, the power output of a single SMR was dispatched to compensate for the wind generation variations in [15]. Besides, heating extraction and reactor maneuvring were coordinated in [16] for optimal load following in a hybrid energy system. In terms of simulation, the operation of a nuclear-renewable hybrid energy system under different scenarios was demonstrated through real-time simulators [17].

Even though much work has been done on the modeling, control, scheduling, and simulation of SMRs, the planning issue of SMRs has rarely been touched. In standalone system planning with SMRs, the operational characteristics and regulation constraints of SMRs need to be analyzed and included. On this basis, SMRs and other available resources are coordinated to provide a reliable power supply for a given deployment scenario. Apart from the coordination of steady-state power output for power-supply balance, the coordination of dynamic frequency response also needs to be integrated, which is essential for maintaining *frequency security* under sudden power imbalances [18]. Although the dynamic response of SMRs in providing frequency regulation services has been preliminarily investigated in the literature, the coordination of SMRs with the power electronic interfaced sources for frequency regulation is still an open question. In particular, the investment capacity of SMRs and other resources needs to be determined to ensure the frequency security of the SMR-renewable integrated energy system.

The mainstream to incorporate dynamic frequency security issues in steady-state operation/planning is to formulate frequency security requirements as constraints in the optimization model. However, integrating non-linear frequency security constraints leads to high computational complexity [19]. Different methodologies have been proposed to overcome the challenge, including linearization, non-linear optimization, and heuristic methods. In [20], the limitation on Rate-of-change-of-Frequency (RoCoF), steady-state deviation, and frequency nadir were linearized with piecewise linearization and integrated into the unit commitment (UC) problem. Thereby, the mixed-integer linear formulation of the UC model was preserved. A similar idea was introduced in [21], where deep neural networks were trained to represent the frequency nadir as linear constraints and incorporated into the UC problem. Nonlinear optimization could be adopted in case the constraints were converted into specific forms. For example, the frequency constraints were derived and formulated into a second-order cone form. In this case, the frequency-constrained microgrid scheduling problem could be solved analytically [22]. A three-stage tractable heuristic solution method was proposed in [23] for the frequency-constrained microgrid planning, where the dynamic frequency security of microgrids was guaranteed by iteratively tightening the bounds.

There are two challenges to the frequency-constrained planning of SMR-integrated energy systems. Firstly, from the modeling perspective, the frequency response dynamics of SMR are complex with high-order differential equations, which are challenging to represent accurately through model-based methods. Secondly, from the solution perspective, the frequency security constraints are highly nonlinear and cannot be expressed analytically, which makes it challenging to solve the frequency-constrained planning problem effectively. By addressing these two challenges, this paper makes the following contributions:

1) Establish an optimal planning model of standalone net-zero energy systems with SMRs, where SMRs, PV, battery energy storage, and seasonal energy storage are coordinated to supply local load demand. In the planning model, the dynamic frequency security constraints are represented as requirements on frequency reserves of different resources and incorporated into the steady-state operation constraints.
2) Propose a physics-informed neural network (PINN)-based approach to capture the complex dynamic response of SMR as a transfer function model. The dynamic model is aggregated with other resources in the system to derive the frequency security constraints subjected to sudden power imbalances.
3) Develop an iterative algorithm to solve the planning model with nonlinear frequency security constraints and decision-dependent PV generation, where the nonlinear frequency nadir constraint is gradually satisfied through fast frequency response expansion at each iteration step.

The rest of this paper is organized as follows. Section II introduces the problem studied in this paper; Section III models the dynamic response of SMR in a data-driven way; Section IV formulates the optimal planning model; Section V proposes a two-level iterative solution method; case studies are conducted in Section VI; Section VII concludes the paper.

II. Problem Statement

Fig. 1 illustrates a standalone net-zero energy system that integrates SMRs, PV, battery energy storage (BESS), and seasonal energy storage (SESS, including electrolyzer, fuel cell, and hydrogen storage) to supply local demand. In such a standalone operation mode, the locally available sources need to be coordinated to satisfy the supply-demand balance and sustain system frequency within the required limits.

We aim to determine the portfolio of the net-zero energy system with minimized costs. The problem can be stated as follows: **Given:** (1) the load data and normalized PV output; (2) investment and operation costs of the distributed energy resources (DERs); (3) operation characteristics of DERs. **Determine:** (1) the capacity of DERs to be invested; (2) the optimal operating status (including power output, frequency reserve, etc.).

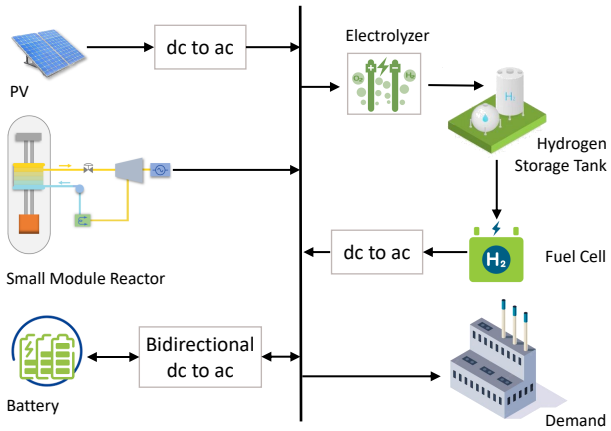

Fig. 1. System diagram of a net-zero energy system with SMRs.

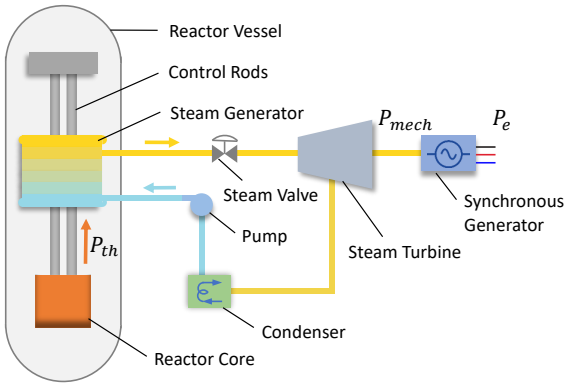

Fig. 2. Simplified structure of a small modular reactor.

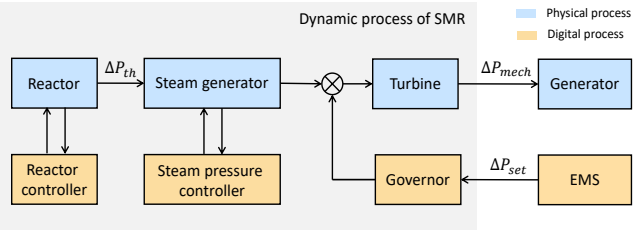

Fig. 3. Dynamic process of SMR in turbine-led operation mode.

Typical days will be first selected to represent the future operational status of DERs in the planning years. On each typical day, SMRs, PV, BESS, and SESS are coordinated to balance the supply and demand on an hourly basis. Meanwhile, the frequency security in a shorter time scale needs to be guaranteed under a power imbalance contingency. In the faster dynamic process, the inertia and frequency regulation supports from the resources are coordinated.

The net-zero planning of the SMR-integrated energy system in this paper differs from the traditional energy system planning problem in two ways: 1) the unique characteristics of SMR are incorporated; 2) the dynamic frequency security requirements are integrated. The challenges and research tasks are threefold:

1) *Complex dynamics:* A data-driven method is employed to identify the dynamic response of SMR for frequency regulation analysis.
2) *Multi-time-scale constraints:* The investment constraints, steady-state operation constraints, and dynamic frequency security constraints are derived and incorporated into the planning model.
3) *High unanalytical model:* A two-level tractable iterative method is proposed to find the solution heuristically.

III. Data-Driven SMR Dynamics Modeling

Fig. 2 shows the balance-of-plant system of SMR. Inside the reactor vessel, the control rods are used to regulate the reactivity in the reactor core and thus adjust the reactor power level P_{th}, which is transferred to the steam generator. The steam then drives the steam turbine to generate mechanical power P_{mech}, which is transmitted to a synchronous generator and produces electrical power P_e. The steam from the turbine outlet is condensed and pumped back to the steam generator.

Basically, SMR can operate in either reactor-led or turbine-led mode. In reactor-led operations, the mechanical power output P_{mech} follows the change of reactor power output P_{th}, which is specified by tuning the control rods. In turbine-led operations, the mechanical power output P_{mech} is adjusted directly by tuning the steam valve. The two operation modes are employed in different time frames. P_{th} is scheduled hourly for the balance of supply and demand, while P_{mech} is adjusted in a faster time scale for frequency regulation [15], [16].

Fig. 3 shows the dynamic process of SMR in turbine-led mode, which includes the physical dynamics of the components and the digital dynamics of the control loops. It should be noted that the transient dynamic response of SMR for frequency regulation is separated from the steady-state operation for hourly supply-demand balance. Compared with the steady-state power output, the dynamic response of SMR for frequency regulation is a small scale deviation denoted as ΔP_{mech}. The input of the dynamic process is the set point ΔP_{set} required for the power output deviation. Denotes the dynamic variables in the whole process as $\Delta \mathbf{x}$. $\Delta \mathbf{x}$ includes the deviation variables in the reactor core, the fuel-coolant heat transfer process, the pressurizer, the steam generator, and the governor-turbine system. Each dynamic variable involves one or more differential equations governed by the physical or digital process. The dynamic process of SMR is finally represented as a 23rd-order state-space model.

Since we focus on the dynamic response of the mechanical power output P_{mech} subjected to the given set point ΔP_{set}, we denote the set point ΔP_{set} as the system input and the mechanical power P_{mech} as the system output. The dynamic process can be transformed into an input-output transfer function model

$$\text{SMR}\,(s) = \frac{\Delta P_{\text{mech}}\,(s)}{\Delta P_{\text{set}}\,(s)} = \frac{b_q s^q + b_{q-1} s^{q-1} + \ldots + b_0}{a_p s^p + a_{p-1} s^{p-1} + \ldots + a_0} \tag{1}$$

where s denotes the Laplacian operator. p and q denote the model order. The model parameters a_i $(i = 0, \ldots, p)$ and b_j $(j = 0, \ldots, q)$ are associated with SMR dynamics.

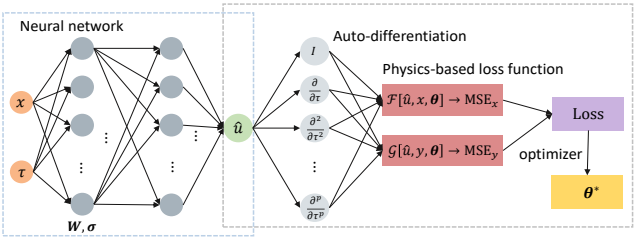

Fig. 4. The schematics of PINN-based SMR dynamic response identification.

However, the derivation of the system model relies on detailed and accurate parameters of the physical components and control loops, which are hard to obtain. Operational data are collected and used to identify the model parameters. Data-driven parameter estimation can be achieved by traditional system identification methods, such as the System Identification Toolbox in MATLAB. However, the input signal ΔP_{set} is required to be time-varying within the dynamic process (usually a few seconds). Since the input signal ΔP_{set} is set by the Energy Management System (EMS) according to the variation of load, it could not change frequently in the seconds time scale. In real-time operation, ΔP_{set} is usually adjusted after the system returns to steady-state, which forms multiple sets of step responses.

In this case, an emerging data-driven method, PINN, is adopted to estimate the model parameters [24], [25]. In the PINN sets, neural networks are used to approximate the system output, where the physical model (1) is incorporated into the training procedure [26]. In the following, the detailed application of PINN to the SMR dynamic identification is explained.

For simplicity, denote ΔP_{set} and ΔP_{mech} as x and y, respectively, the transfer function model (1) can be rewritten in the time-domain formulation of a differential equation

$$\begin{aligned} &a_p y^{(p)}(\tau) + a_{p-1} y^{(p-1)}(\tau) + \ldots + a_0 y(\tau) = \\ &b_q x^{(q)}(\tau) + b_{q-1} x^{(q-1)}(\tau) + \ldots + b_0 x(\tau), \end{aligned} \tag{2}$$

where τ represents the time in the dynamic process. We aim to estimate the model parameters a_i $(i = 0, \ldots, p)$ and b_j $(j = 0, \ldots, q)$ through the collected data.

Multiple sets of step response data are collected as the input of the PINN training process. When there is a change ΔP_{set} (x) in the set point of SMR's power output, the dynamic response of the SMR's power output ΔP_{mech} (y) in the following time horizon τ is recorded. Multiple such trajectories formulate the training dataset. To integrate (2) into the PINN training process with multiple sets of step responses, the time derivatives of the input $x(\tau)$ need to be transformed. An auxiliary variable $u(\tau)$ is introduced and (2) is rewritten as

$$a_p u^{(p)}(\tau) + a_{p-1} u^{(p-1)}(\tau) + \ldots + a_0 u(\tau) = x(\tau), \tag{3a}$$

$$b_q u^{(q)}(\tau) + b_{q-1} u^{(q-1)}(\tau) + \ldots + b_0 u(\tau) = y(\tau). \tag{3b}$$

The schematics of PINN-based SMR dynamic identification are illustrated in Fig. 4. System input x and the transient time point τ are the inputs of the neural networks. The output of neural network $\hat{u}$ is the estimate of the auxiliary variable u at time τ. For each input data x and τ, the auxiliary variable u is calculated as

$$\begin{cases} [x, \tau]^{\mathrm{T}} = \mathbf{z}_0, \\ \mathbf{z}_{l+1} = \boldsymbol{g}\left(\boldsymbol{W}_l \mathbf{z}_l + \boldsymbol{\sigma}_l\right), \ \forall l = 0, \ldots, l_{\mathrm{n}} - 1, \\ \hat{u} = \boldsymbol{W}_{l_{\mathrm{n}}} \mathbf{z}_{l_{\mathrm{n}}} + \boldsymbol{\sigma}_{l_{\mathrm{n}}}, \end{cases} \tag{4}$$

where $\mathbf{z}_l$ is the output variable of the network at layer l. $\boldsymbol{W}_l$ and $\boldsymbol{\sigma}_l$ are the weight matrix and bias vector of the neural network at layer l, respectively. $\boldsymbol{g}(\cdot)$ is the activation function of the neural network. l_n is the number of the network layers. Apart from the neural network-related variables $\boldsymbol{W}$ and $\boldsymbol{\sigma}$, the unknown system parameters a_i and b_j are treated as additional parameters $\boldsymbol{\theta}$. In the training process, $\boldsymbol{W}$, $\boldsymbol{\sigma}$ and $\boldsymbol{\theta}$ are estimated that yield the best agreement of the underlying two physical equations in (3). This forms the following physics-informed loss functions

$$\begin{cases} \mathcal{F}[\cdot] = \hat{a}_p \hat{u}^{(p)}(\tau) + \hat{a}_{(p-1)} \hat{u}^{p-1}(\tau) + \ldots + \hat{a}_0 \hat{u}(\tau) - x(\tau) \\ \mathcal{G}[\cdot] = \hat{b}_q \hat{u}^{(q)}(\tau) + \hat{b}_{q-1} \hat{u}^{(q-1)}(\tau) + \ldots + \hat{b}_0 \hat{u}(\tau) - y(\tau), \end{cases} \tag{5}$$

where the derivatives of $\hat{u}$ are obtained through the auto-differentiation function. Given N_c as the number of training data, the total loss function Loss is formulated as

$$\text{Loss} = \frac{1}{N_c} \sum_{c=1}^{N_c} \left(\mathcal{F}[\hat{u}_c, x_c, \boldsymbol{\theta}]^2 + \mathcal{G}[\hat{u}_c, y_c, \boldsymbol{\theta}]^2 \right). \tag{6}$$

By minimizing the total loss function Loss over the neural network related variables $\boldsymbol{W}$, $\boldsymbol{\sigma}$ and system parameters $\boldsymbol{\theta}$, the estimates the of the system parameters can be obtained

$$\boldsymbol{\theta}^* = \underset{\boldsymbol{W}, \boldsymbol{\sigma}, \boldsymbol{\theta}}{\arg\min}\, \text{Loss}. \tag{7}$$

Problem (7) can be solved by using Adam optimizer [27], a stochastic optimization method. The Adam optimizer is widely used for training neural networks due to its ability to adapt learning rates during training, which often leads to faster convergence and better optimization results. Through the PINN-based identification process, the model parameters in (1) can be obtained.

Remark 1: Different from the existing studies that primarily focus on modeling nuclear generation dynamics and stability analysis, we employ a data-driven approach to capture the dynamics of SMRs as a reduced-order model. In this case, we simplify the dynamic coordination of SMRs with power electronics interfaced resources, facilitating the integration of frequency security constraints into the capacity planning problem. Furthermore, the proposed data-driven modeling framework is also adaptable to large-scale nuclear power plants, which could be utilized in capacity planning of nuclear-renewable energy systems.

IV. Optimal Planning Model

This section mathematically formulates the planning model, including the objective function, investment constraints, steady-state operation constraints, and dynamic frequency security constraints.

A. Objective Function

The objective is to minimize the overall cost π, including the investment cost π^I and operation cost π^O of the DERs

$$\min \ \pi = \pi^I + \pi^O. \tag{8}$$

Specifically, the π^I and π^O are represented as

$$\begin{aligned} \pi^I &= \textstyle\sum_{m=1}^{M} I^{\mathrm{SMR}} C^{\mathrm{SMR}} X_m + I^{\mathrm{PV}} C^{\mathrm{PV}} + I^{\mathrm{B}} C^{\mathrm{B}} \\ &\quad + I^{\mathrm{S}} C^{\mathrm{S}} + I^{\mathrm{SE}} C^{\mathrm{SE}} \\ \pi^O &= \textstyle\sum_{w=1}^{W} \sum_{t=1}^{T} \sum_{m=1}^{M} \psi_w O^{\mathrm{SMR}} P^{\mathrm{SMR}}_{m,t,w} \end{aligned} \tag{9}$$

where I^{SMR}, I^{PV}, and I^{B} are the annualized investment costs of the SMR, PV, and BESS, respectively. For SMR, the investment cost I^{SMR} includes the construction cost and several other parts specified for the operation of nuclear power plants, e.g. the security cost, decommissioning cost, and insurance cost. For example, the security cost is considered as the installation of multiple security monitoring stations [8]. For SESS, the capabilities of charging/discharging and energy storage are realized by the electrolyzer/fuel cell and hydrogen (H_2) storage, respectively, as shown in Fig. 1. Thus, the investment costs of SESS include the cost of charging/discharging technology I^{S} and the cost of energy storage technology I^{SE}. C^{PV}, C^{B}, C^{S}, and C^{SE} denote the invested capacity of PV, BESS, SESS, and H_2 storage. For SMR, C^{SMR} is the capacity of an SMR module and M is the number of SMR modular candidates. The investment decision of SMR is a binary variable $X_m \in \{0,1\}$ that represents whether SMR modular candidate m is selected. In the planning model, the investment decisions of SMRs are based on whether to invest in a modular candidate. For PV, BESS, SESS, and H_2 storage, given the development of the technologies, the base capacity of such units can be small-scale. We relax the decision variables as continuous variables [28].

The operation cost π^O is the sum of the variable cost of the invested SMR in the whole year, where O^{SMR} is the variable cost of SMR. The variable cost O^{SMR} is a combination of fuel costs and operation and maintenance (O&M) costs. Here we use the concept of "Levelised Cost of Electricity (LCOE)" to represent the variable cost of SMR, which is estimated from large-scale economic analysis of SMRs [29]. $P^{\mathrm{SMR}}_{m,t,w}$ is the power output of SMR m at time step t on typical day w. ψ_w denotes the number of days that the w-th typical day can represent and the sum of ψ_w is equal to 365 days (an entire year). T and W denote the number of time periods (24h) and typical days, respectively.

B. Investment Constraints

The investment capacities of DERs are limited by the locally available resources:

$$0 \le C^{\mathrm{PV}} \le C^{\mathrm{PV}}_{\mathrm{lim}} \tag{10a}$$
$$0 \le C^{\mathrm{B}} \le C^{\mathrm{B}}_{\mathrm{lim}} \tag{10b}$$
$$0 \le C^{\mathrm{S}} \le C^{\mathrm{S}}_{\mathrm{lim}} \tag{10c}$$
$$0 \le C^{\mathrm{SE}} \le C^{\mathrm{SE}}_{\mathrm{lim}} \tag{10d}$$

where $C^{\mathrm{PV}}_{\mathrm{lim}}$, $C^{\mathrm{B}}_{\mathrm{lim}}$, $C^{\mathrm{S}}_{\mathrm{lim}}$ and $C^{\mathrm{SE}}_{\mathrm{lim}}$ denote the maximum capacity of PV, BESS, SESS and H_2 storage that can be invested.

C. Steady-State Operation Constraints

The operation characteristics of DERs and supply-demand balance on an hourly basis are represented as steady-state operation constraints in this part, which must be satisfied at each time step t on each typical day w.

1) PV: PV is considered to operate at de-loading mode with power reserve for frequency regulation [30].

$$P^{\mathrm{PV}}_{t,w} + R^{\mathrm{PV}}_{t,w} \le \lambda^{\mathrm{PV}}_{t,w} C^{\mathrm{PV}} \tag{11a}$$
$$P^{\mathrm{PV}}_{t,w} - R^{\mathrm{PV}}_{t,w} \ge 0 \tag{11b}$$
$$0 \le R^{\mathrm{PV}}_{t,w} \le r^{\mathrm{PV}}_{\max} \lambda^{\mathrm{PV}}_{t,w} C^{\mathrm{PV}} \tag{11c}$$

Constraints (11a)-(11b) are the power output limits of PV, where $R^{\mathrm{PV}}_{t,w}$ represents the frequency reserve and $\lambda^{\mathrm{PV}}_{t,w}$ denotes the normalized available output of PV. Constraint (11c) restricts the maximum frequency reserve of PV within $r^{\mathrm{PV}}_{\max}$ of the maximum output.

2) SMR: The operation of SMR is constrained by design-specific requirements:

$$P^{\mathrm{SMR}}_{m,t,w} + R^{\mathrm{SMR}}_{m,t,w} \le C^{\mathrm{SMR}} X_m \tag{12a}$$
$$P^{\mathrm{SMR}}_{m,t,w} - R^{\mathrm{SMR}}_{m,t,w} \ge \lambda^{\mathrm{SMR}}_{\min} C^{\mathrm{SMR}} X_m \tag{12b}$$
$$0 \le R^{\mathrm{SMR}}_{m,t,w} \le r^{\mathrm{SMR}}_{\max} C^{\mathrm{SMR}} X_m \tag{12c}$$
$$P^{\mathrm{SMR}}_{m,t,w} - P^{\mathrm{SMR}}_{m,t-1,w} \le \alpha^{\mathrm{Ru}} C^{\mathrm{SMR}} \tag{12d}$$
$$P^{\mathrm{SMR}}_{m,t-1,w} - P^{\mathrm{SMR}}_{m,t,w} \le \alpha^{\mathrm{Rd}} C^{\mathrm{SMR}} \tag{12e}$$
$$\left| P^{\mathrm{SMR}}_{m,t,w} - P^{\mathrm{SMR}}_{m,t-1,w} \right| \le z_{m,t,w} \Pi \tag{12f}$$
$$\left| P^{\mathrm{SMR}}_{m,t,w} - P^{\mathrm{SMR}}_{m,t-1,w} \right| \ge (z_{m,t,w} - 1)\,\Pi + \Theta \tag{12g}$$
$$\sum_{t=1}^{T} z_{m,t,w} \le Z_{\mathrm{lim}}. \tag{12h}$$

Constraints (12a)-(12b) are the power output limits of SMR [3], where $R^{\mathrm{SMR}}_{m,t,w}$ is the reserve for frequency regulation [31]. $\lambda^{\mathrm{SMR}}_{\min}$ is the minimum rate of power output. Constraint (12c) ensures that the frequency reserve of SMR remains within $r^{\mathrm{SMR}}_{\max}$ of the rated power [32]. Constraints (12d)-(12e) formulates the ramp limits [15], where α^{Ru} and α^{Rd} represent the ramp-up/down rates. Since the thermal and operational cycling caused by reactor power maneuvering will result in the degradation of components and lower module availability, the changes in reactor output in one day are restricted [16]. Constraints (12f)-(12h) guarantee the number of changes of reactor power in one day is no more than Z_{lim}, where $z_{m,t,w} \in \{0,1\}$ is a binary variable representing the adjustment action of reactor power. Π/Θ is an auxiliary large/small number.

It should be noted that the power output $P^{\mathrm{SMR}}_{m,t,w}$ is scheduled on an hourly basis to satisfy the supply-demand balance through the control rod adjustment. $P^{\mathrm{SMR}}_{m,t,w}$ is restricted by (12a)-(12b) to reserve power output $R^{\mathrm{SMR}}_{m,t,w}$ for frequency regulation. For the transient frequency regulation process, the power output of SMR can be changed through the turbine-led mode with a maximum value of $R^{\mathrm{SMR}}_{m,t,w}$.

3) BESS: BESS works as a flexible resource to compensate for daily load and renewable variations. Meanwhile, taking

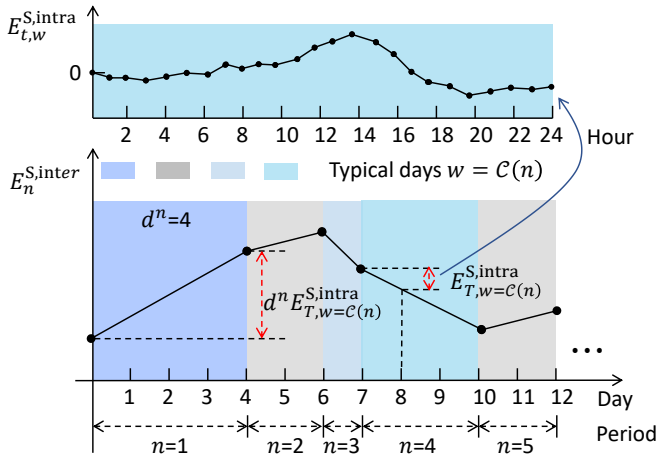

Fig. 5. Chronological SoC of SESS with inter-day coupling.

advantage of the fast dynamics, BESS could be employed to provide frequency reserve [33].

$$0 \le P^{\mathrm{B}+}_{t,w} \le x^{\mathrm{B}+}_{t,w}(C^{\mathrm{B}} - R^{\mathrm{B}}_{t,w}) \tag{13a}$$
$$0 \le P^{\mathrm{B}-}_{t,w} \le x^{\mathrm{B}-}_{t,w}(C^{\mathrm{B}} - R^{\mathrm{B}}_{t,w}) \tag{13b}$$
$$x^{\mathrm{B}+}_{t,w} + x^{\mathrm{B}-}_{t,w} \le 1,\ x^{\mathrm{B}+}_{t,w} \in \{0,1\},\ x^{\mathrm{B}-}_{t,w} \in \{0,1\} \tag{13c}$$
$$0 \le R^{\mathrm{B}}_{t,w} \le r^{\mathrm{B}}_{\max} C^{\mathrm{B}} \tag{13d}$$
$$E^{\mathrm{B}}_{t,w} = (1-\gamma^{\mathrm{B}})E^{\mathrm{B}}_{t-1,w} + P^{\mathrm{B}+}_{t,w}\eta^{\mathrm{B}+} - P^{\mathrm{B}-}_{t,w}/\eta^{\mathrm{B}-} \tag{13e}$$
$$E^{\mathrm{B}}_{0,w} = E^{\mathrm{B}}_{T,w} = \lambda^{\mathrm{B}}_{\mathrm{ini}}\kappa^{\mathrm{B}}C^{\mathrm{B}} \tag{13f}$$
$$E^{\mathrm{B}}_{\min} \le E^{\mathrm{B}}_{t,w} \le \kappa^{\mathrm{B}}C^{\mathrm{B}} \tag{13g}$$

Constraints (13a)-(13c) limit the charging/discharging power $P^{\mathrm{B}+}_{t,w}/P^{\mathrm{B}-}_{t,w}$ of BESS, where $x^{\mathrm{B}+}_{t,w}$ and $x^{\mathrm{B}-}_{t,w}$ are binary variables that represent the charging/discharging state. Constraint (13d) restricts the frequency reserve rate of BESS within $r^{\mathrm{B}}_{\max}$ of rated power. Constraint (13e) represents the energy balance of BESS, where $E^{\mathrm{B}}_{t,w}$, γ^{B}, and $\eta^{\mathrm{B}+}/\eta^{\mathrm{B}-}$ denote the SoC, self-discharging rate and charging/discharging efficiency. Constraint (13f) ensures that SoC at the final time step of one day is equal to the initial SoC [28], where κ^{B} is the energy capacity coefficient and $\lambda^{\mathrm{B}}_{\mathrm{ini}}$ is the initial SoC rate. Constraint (13g) imposes the upper (energy capacity $\kappa^{\mathrm{B}}C^{\mathrm{B}}$) and lower ($E^{\mathrm{B}}_{\min}$) limits on the SoC.

4) SESS: Compared with BESS, SEES can compensate for the inter-day supply-demand balance. In this case, the sequence of different typical days in one year needs to be adopted [34]. As shown in Fig. 5, the 365 days of a year are separated into N periods (indexed as n) according to the typical days and their sequence. The days in each period n can be represented by the same typical day $w = \mathcal{C}(n)$. The number of days in period n is denoted as d^n. We employ the method in [35] to separate the SoC of SESS with intra-day state $E^{\mathrm{S,intra}}_{t,w}$ and inter-day state $E^{\mathrm{S,inter}}_{n}$ to derive the coupling of SoC among different typical days.

$$0 \le P^{\mathrm{S}+}_{t,w} \le x^{\mathrm{S}+}_{t,w}C^{\mathrm{S}} \tag{14a}$$
$$0 \le P^{\mathrm{S}-}_{t,w} \le x^{\mathrm{S}-}_{t,w}C^{\mathrm{S}} \tag{14b}$$
$$x^{\mathrm{S}+}_{t,w} + x^{\mathrm{S}-}_{t,w} \le 1,\ x^{\mathrm{S}+}_{t,w} \in \{0,1\},\ x^{\mathrm{S}-}_{t,w} \in \{0,1\} \tag{14c}$$
$$E^{\mathrm{S}}_{t,d,n} = E^{\mathrm{S,inter}}_{n-1} + (d-1)E^{\mathrm{S,intra}}_{T,w=\mathcal{C}(n)} + E^{\mathrm{S,intra}}_{t,w=\mathcal{C}(n)} \tag{14d}$$
$$E^{\mathrm{S,intra}}_{0,w} = 0,\ E^{\mathrm{S,inter}}_{0} = E^{\mathrm{S,inter}}_{N} = \lambda^{\mathrm{S}}_{\mathrm{ini}}C^{\mathrm{SE}} \tag{14e}$$
$$E^{\mathrm{S,intra}}_{t,w} = E^{\mathrm{S,intra}}_{t-1,w} + P^{\mathrm{S}+}_{t,w}\eta^{\mathrm{S}+} - P^{\mathrm{S}-}_{t,w}/\eta^{\mathrm{S}-} \tag{14f}$$
$$E^{\mathrm{S,inter}}_{n} = E^{\mathrm{S,inter}}_{n-1} + d^n E^{\mathrm{S,intra}}_{T,w=\mathcal{C}(n)} \tag{14g}$$
$$0 \le E^{\mathrm{S}}_{t,d,n} \le C^{\mathrm{SE}} \tag{14h}$$

Constraints (14a)-(14c) represents the charging/discharging $P^{\mathrm{S}+}_{t,w}/P^{\mathrm{S}-}_{t,w}$ limitations of SESS, where $x^{\mathrm{S}+}_{t,w}$ and $x^{\mathrm{S}-}_{t,w}$ are binary variables that represent the charging/discharging state. Constraint (14d) indicates the SoC $E^{\mathrm{S}}_{t,d,n}$ includes the inter-day SoC $E^{\mathrm{S,inter}}_{n-1}$, the SoC change of the previous $d-1$ days, and the intra-day $E^{\mathrm{S,intra}}_{t,w=\mathcal{C}(n)}$ at time t on day d. The initial intra-day SoC is assumed to be 0 and constraint (14e) ensures the SoC at the end of the year returns to the initial value, where $\lambda^{\mathrm{S}}_{\mathrm{ini}}$ denotes the initial SoC rate. Constraint (14f) represents the intra-day energy balance of SESS, where $\eta^{\mathrm{S}+}/\eta^{\mathrm{S}+}$ denote the charging/discharging efficiency. Constraint (14g) represents the SoC change in the whole period n, which is also illustrated in Fig. 5. Constraint (14h) limits the SoC at each time step within the capacity. The frequency support from SESS is not considered in this study.

5) Demand-supply Balance:

$$\sum_{m=1}^{M} P^{\mathrm{SMR}}_{m,t,w} + P^{\mathrm{PV}}_{t,w} + P^{\mathrm{B}-}_{t,w} + P^{\mathrm{S}-}_{t,w} = L_{t,w} + P^{\mathrm{B}+}_{t,w} + P^{\mathrm{S}+}_{t,w} \tag{15}$$

Constraint (15) ensures the balance between the supply and load demand $L_{t,w}$ at each time step.

6) System Capacity Reserve: The system is required to provide capacity reserves for unexpected contingencies during operation. For example, the uncertainty of load/PV generation, or the outage of a power plant. The maximum available generation needs to be more than the sum of the load demand plus the required reserve at each time step. Considering the uncertainty of load and PV generation, the capacity reserve constraint is formulated as

$$\sum_{m=1}^{M} C^{\mathrm{SMR}}X_m + \lambda^{\mathrm{PV}}_{t,w}C^{\mathrm{PV}} + C^{\mathrm{B}} + C^{\mathrm{S}} \ge \left(1+e^{L}\right)L_{t,w} + e^{\mathrm{PV}}\lambda^{\mathrm{PV}}_{t,w}C^{\mathrm{PV}}, \tag{16}$$

where e^{L} and e^{PV} represent the uncertainty level of load and PV generation, respectively. Note that the required reserve is designed by the system operator, which can be set much larger to withstand outages of power plants or BESS.

D. Dynamic Frequency Security Constraints

Apart from the steady-state operation constraints, the system frequency is required to be sustained within specific limits under sudden power imbalances. With this aim, sufficient system inertia and frequency regulation support need to be guaranteed. In this part, the frequency security constraints are derived through the transfer function model and represented

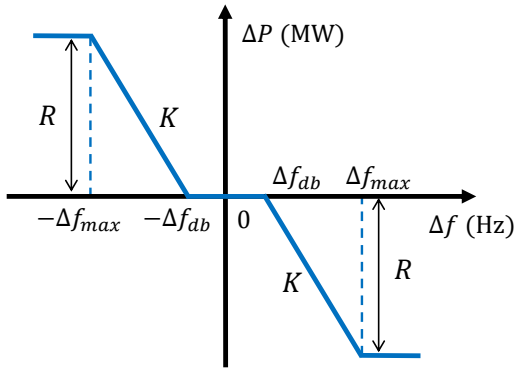

Fig. 6. P-f droop characteristics of frequency regulation.

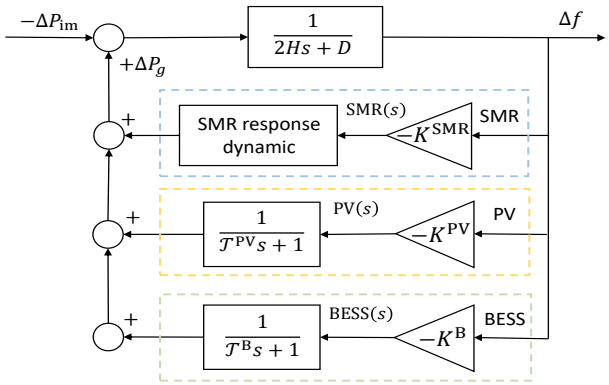

Fig. 7. Transfer function model of system frequency response.

as requirements on frequency reserves, through which the dynamic performance of frequency is guaranteed.

The frequency dynamics after a sudden contingency (power imbalance) $\Delta P_{\rm im}$ is presented as:

$$2H\frac{d\Delta f(\tau)}{d\tau} + D\Delta f(\tau) = \Delta P_g(\tau) - \Delta P_{\rm im}(\tau), \quad (17)$$

where τ represents the time in the frequency dynamic process; H and D are the system inertia and load-damping constant; Δf is the deviations of frequency. ΔP_g is the primary frequency response from the frequency support resources SMR, PV, and BESS. Typically, for each resource, a power-frequency (P-f) droop controller is adopted for primary frequency regulation. Take SMR as an example, the characteristics of the P-f droop controller are illustrated in Fig. 6. The frequency control dead bound $\Delta f_{\rm db}$ is set to avoid unnecessary frequency response. After the frequency deviation surpasses the frequency control dead bound, the primary frequency response is activated, and the frequency response ΔP changes proportionally to the frequency deviation Δf. Here the value of the frequency control dead bound is chosen as 0.016Hz, which is commonly used in the literature [36].

The dynamic frequency security requirements include the limitation on the maximum RoCoF $|\Delta f'|_{\max}$, the steady-state frequency deviation $|\Delta f_{\rm ss}|$ and frequency nadir $|\Delta f|_{\max}$. The frequency responses $\Delta P_g(\tau)$ from SMR, PV, and BESS are provided through the droop controller $K^{\rm SMR}$, $K^{\rm PV}$, and $K^{\rm B}$, respectively. The dynamic response of SMR is identified as $\mathrm{SMR}(s)$ through the method in Section III. PV and BESS are connected to the system through power electronic devices and the dynamic responses are represented as first-order transfer functions with specific time constants $\mathcal{T}^{\rm PV}$ and $\mathcal{T}^{\rm B}$ [19]. The detailed transfer function model of frequency dynamic is shown in Fig. 7.

The capability of frequency regulation supports from DERs is associated with the frequency reserve [18]. Specifically, SMR provides inherent inertia and droop gain for the system

$$H^{\rm SMR} = \sum_{m=1}^{M} C^{\rm SMR} H_m X_m / f_0 \quad (18a)$$

$$K_{t,w}^{\rm SMR} = \sum_{m=1}^{M} R_{m,t,w}^{\rm SMR} / |\Delta f|_{\max,\lim} \quad (18b)$$

where $H^{\rm SMR}$ denotes the inertia support from SMRs. H_m is the inertia constant of a single SMR module. f_0 is the nominal value of system frequency. The droop gain $K_{t,w}^{\rm SMR}$ is determined by the sum of frequency reserve $R_{m,t,w}^{\rm SMR}$ and the maximum acceptable frequency deviation $|\Delta f|_{\max,\lim}$. It should be noted that since the frequency control dead bound (0.016Hz) is relatively small compared with the maximum acceptable frequency deviation $|\Delta f|_{\max,\lim}$ (0.8Hz), we relax the impact of frequency control dead bound on droop gain and use (18b) to calculate the droop gain.

The power electronic interfaced resources PV and BESS are considered to provide both synthetic inertial and primary frequency responses [37]

$$2H_{t,w}^{\rm PV}|\Delta f'|_{\max,\lim} + K_{t,w}^{\rm PV}|\Delta f|_{\max,\lim} = R_{t,w}^{\rm PV}, \quad (19a)$$

$$2H_{t,w}^{\rm B}|\Delta f'|_{\max,\lim} + K_{t,w}^{\rm B}|\Delta f|_{\max,\lim} = R_{t,w}^{\rm B}, \quad (19b)$$

where the synthetic inertia and droop gain are associated with the maximum acceptable RoCoF $|\Delta f'|_{\max,\lim}$ and maximum acceptable frequency deviation $|\Delta f|_{\max,\lim}$, respectively.

In the following, the three frequency security constraints associated with the planning/operation decisions are derived.

1) Rate of Change of Frequency Constraint:

$$|\Delta f'|_{\max} = \left|-\frac{\Delta P_{\rm im}}{2H_{t,w}}\right| \le |\Delta f'|_{\max,\lim} \quad (20)$$

where the system inertia $H_{t,w}$ includes the inherent inertia from SMR and the real-time synthetic inertia from the frequency reserve of PV and BESS

$$H_{t,w} = H^{\rm SMR} + H_{t,w}^{\rm PV} + H_{t,w}^{\rm B}. \quad (21)$$

2) Steady-state Frequency Deviation Constraint:

$$|\Delta f_{\rm ss}| = \left|\frac{\Delta P_{\rm im}}{D + K_{t,w}}\right| \le |\Delta f_{\rm ss}|_{\lim} \quad (22)$$

The quasi-steady-state frequency is obtained by assuming that the Laplacian operator s of the transfer function model is zero. The damping coefficient D is assumed a constant irrespective of the load level [19]. The aggregated droop gain K is the sum of droop gains from SMR, PV, and BESS:

$$K_{t,w} = K_{t,w}^{\rm SMR} + K_{t,w}^{\rm PV} + K_{t,w}^{\rm B}. \quad (23)$$

3) Frequency Nadir Constraint:

$$|\Delta f|_{\max} \leq |\Delta f|_{\max,\lim} \tag{24}$$

The nadir point of system frequency $|\Delta f|_{\max}$ represents the maximum deviation of the nominal value. As in Fig. 7, the time response of Δf after a load disturbance ΔP_{im} can be derived through inverse-Laplace transformation as

$$\Delta f(\tau) = \mathcal{L}^{-1}\left\{\frac{\Delta P_{\mathrm{im}}(s)}{2H_{t,w}s + D + \mathrm{PFR}_{t,w}(s)}\right\}, \tag{25}$$

where the $\mathrm{PFR}_{t,w}(s)$ is represented as

$$\mathrm{PFR}_{t,w}(s) = K^{\mathrm{SMR}}_{t,w}\mathrm{SMR}(s) + K^{\mathrm{PV}}_{t,w}\mathrm{PV}(s) + K^{\mathrm{B}}_{t,w}\mathrm{BESS}(s). \tag{26}$$

The analytical expression of the time-domain frequency evolution $\Delta f(\tau)$ can be derived through symbolic computation in MATLAB. The frequency nadir $|\Delta f|_{\max}$ is the absolute value of the extreme point of the time response $\Delta f(\tau)$.

Equations (18)-(26) formulate the frequency security constraints as requirements on system inertia and frequency regulation support, which are associated with the frequency reserve of different resources. It can be seen that all three frequency security constraints are determined by the pre-defined power imbalance ΔP_{im}. In practice, the unexpected power imbalance contingency includes load uncertainty, PV generation uncertainty, and the outages of power plants/BESS. In this case, the pre-defined power imbalance ΔP_{im} can be set artificially to guarantee frequency security for specific scenarios. Different from the work in [18], which assumed a fixed rate of frequency reserve (10% of rated power), the frequency reserves in this study are variables that could be optimized. In this case, the operation flexibility could be improved.

E. Complexity Analysis

The planning model (8) with steady-state operation constraints (9)-(15) is an MILP problem, which could be solved by commercial solvers. The frequency security constraints (20)-(23) are linear constraints that could be integrated into the MILP problem. However, the time response of $\Delta f(\tau)$ derived from (25) is highly nonlinear and it is challenging to get the analytical solution of frequency nadir $|\Delta f|_{\max}$. Thus, the planning model can not be solved directly with the nonlinear constraint (24). Linearization method such as piecewise linearization is proposed in the literature to integrate the frequency nadir constraint into the MILP planning model. However, the frequency response model is simplified and the computational complexity would increase with the associated linearization parameters. To this end, a heuristic solution algorithm is proposed in the following section.

V. Solution Algorithm

This section proposes a heuristic approach to solve the above planning model with two iteration loops, as shown in Fig. 8. The first iteration loop (inner iteration) adapts a "checking and adjusting" strategy to consider the nonlinear frequency nadir constraint (24); the second iteration loop (outer iteration) is used to guarantee the representativeness of the typical daily net load profile considering decision-dependent PV generation. The details are presented in the following.

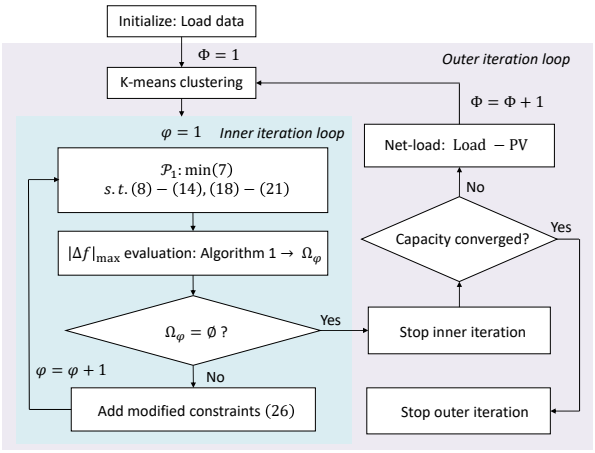

Fig. 8. Proposed two-level iteration solution scheme for the planning model.

A. MILP Planning Problem Solution

Initially, load data of the year is used to get the typical days through the k-means method. The load and normalized available PV output of the typical days form the inputs of the inner iteration process. At the first stage of inner iteration, the objective function (8) together with investment constraints (9)-(10), steady-state operation constraints (12)-(15), and linear frequency security constraints (20)-(23) is formulated as an MILP problem

$$\begin{aligned} \mathcal{P}_1: \min\ & (8) \\ \text{s.t.}\ & (9)-(15), (20)-(23), \end{aligned} \tag{27}$$

which could be easily solved by mature commercial solvers such as Gurobi. The outputs include the investment decisions (the capacities of SMR, PV, BESS, SESS, and $\mathrm{H_2}$ storage) and the operation decisions (the hourly power output and frequency reserve) of different resources at each time step t, w.

B. Frequency Nadir Constraint Checking

The operation decisions of the first-stage planning model are used to evaluate the frequency nadir constraint (24). Based on the inertia (21) and frequency response (26) of the DERs, the frequency nadir $|\Delta f|_{\max}$ is estimated through (25) and Newton iteration. The process is shown in **Algorithm 1**. In this study, the tolerance ϵ is 10^{-6}.

The frequency nadir at each time step of the planning horizon is checked. Each time step t, w that the frequency nadir violates the constraint (24) is included in set Ω_φ, where φ denotes the inner iteration step.

C. Fast Frequency Response Adjustment

As constraints (20) and (22) pose requirements for the system inertia $H_{t,w}$ and aggregated droop gain $K_{t,w}$, the possible

Algorithm 1 Newton iteration for frequency nadir

Input: Tolerance ϵ

Initialize $\Delta f(0) \leftarrow 0$, $\xi \leftarrow 0$
repeat
  $\xi \leftarrow \xi + 1$
  $\Delta f(\xi) \leftarrow \Delta f(\xi-1) - \Delta f'(\xi-1) / \Delta f''(\xi-1)$
until $|\Delta f(\xi) - \Delta f(\xi-1)| < \epsilon$
$\Delta f^* \leftarrow \Delta f(\xi)$

Output: Frequency nadir $|\Delta f|_{\max} \leftarrow |\Delta f^*|$

TABLE I
SENSITIVITY ANALYSIS OF SYSTEM PARAMETERS TO FREQUENCY NADIR

Parameter ϑ	Inertia (MWs/Hz)	Droop gain (MW/Hz)		
	H	K^{SMR}	K^{PV}	K^{B}
min value*	0.5	0	0	0
max value*	0.9	1.25	0.75	0.5
$\lvert\Delta f\rvert_{\max}/\Delta\vartheta$	-0.025	-0.043	-0.113	-0.131

* Parameters values are based on Case Study in Section VI.

reason that leads to the violation of frequency nadir constraint in Ω_φ is the lacking of frequency response before the nadir time. That is, the fast frequency response is insufficient. As SMR is a turbine-based source with a larger time constant, the faster frequency response from power electronic interfaced resources in Ω_φ need to be enhanced. Besides, sensitivity analysis is conducted based on Monte Carlo simulation to confirm the dominant factor that would affect the frequency nadir. The results of sensitivity analysis are shown in Table I.

From the sensitivity analysis result, the power electronic interfaced resources with faster response time have a greater impact on the frequency nadir. Thus, it is reasonable to expand the droop gains of PV and BESS in Ω_φ in the next iteration step $\varphi+1$ to improve the frequency response performance

$$\begin{aligned}
&\left[K^{\mathrm{PV}}_{t,w} + K^{\mathrm{B}}_{t,w}\right]_{\varphi+1} \geq (1+\mu)\left[K^{\mathrm{PV}}_{t,w} + K^{\mathrm{B}}_{t,w}\right]_{\varphi} \forall t,w \in \Omega_\varphi \\
&\left[K^{\mathrm{PV}}_{t,w} + K^{\mathrm{B}}_{t,w}\right]_{\varphi+1} \geq \left[K^{\mathrm{PV}}_{t,w} + K^{\mathrm{B}}_{t,w}\right]_{\varphi} \ \forall t,w \notin \Omega_\varphi \\
&\left[K^{\mathrm{SMR}}_{t,w}\right]_{\varphi+1} \geq \left[K^{\mathrm{SMR}}_{t,w}\right]_{\varphi} \ \forall t,w \\
&\left[H_{t,w}\right]_{\varphi+1} \geq \left[H_{t,w}\right]_{\varphi} \ \forall t,w
\end{aligned} \tag{28}$$

where μ is the scaling factor used to expand the fast frequency response from PV and BESS. In this work, μ is heuristically selected as 0.02 in our studies to balance the computational efficiency and the optimality. With the modified frequency response requirement (28), the original planning problem $\mathcal{P}_1$ is resolved to improve the frequency performance in Ω_φ where the frequency nadir constraint (24) is violated. In this case, the frequency nadir $|\Delta f|_{\max}$ in Ω_φ will gradually converge within the security limit after several iterations. The inner iteration process is also presented in **Algorithm 2**.

The convergence of **Algorithm 2** can be guaranteed theoretically. As in (28), in case there exist frequency nadir constraint violations, the fast frequency reserve from PV and BESS is expanded. Other frequency supports like system inertia and frequency regulation service from SMR are maintained at least the same. Thus, the frequency nadir is monotonically decreasing at each iteration step of **Algorithm 2**. The fast frequency reserve from BESS and PV are associated with their investment capacity, which is supposed to be sufficient. Thereby, in the end, the frequency nadir constraint will be satisfied at all time steps.

Algorithm 2 Three-stage solution for the frequency-security constrained planning problem

Input: Load and normalized PV output of typical days.

Iteration step: $\varphi \leftarrow 1$
Initialize the investment decisions $\left\{X_m, C^\beta\right\}_\varphi$, operation decisions $\left\{P^{\mathrm{SMR}}_{m,t,w}\right\}_\varphi$, $\left\{P^{\chi}_{t,w}\right\}_\varphi$, $\left\{R^{\varpi}_{t,w}\right\}_\varphi$ [1] by solving $\mathcal{P}_1$
repeat
  Derive $|\Delta f|_{\max}$ via (25), (26) and **Algorithm 1** at each time step t, w
  if $|\Delta f|_{\max} > |\Delta f|_{\max,\lim}$ **then**
    $\Omega_\varphi \leftarrow \Omega_\varphi \cup (t,w)$
  end if
  $\varphi \leftarrow \varphi + 1$
  Update investment decisions $\left\{X_m, C^\beta\right\}_\varphi$, operation decisions $\left\{P^{\mathrm{SMR}}_{m,t,w}\right\}_\varphi$, $\left\{P^{\chi}_{t,w}\right\}_\varphi$, $\left\{R^{\varpi}_{t,w}\right\}_\varphi$ by resolving $\mathcal{P}_1$ with additional constraints (28)
until $\Omega_\varphi = \emptyset$

Output: Optimal investment decisions $\left\{X_m, C^\beta\right\}_\varphi$, operation decisions $\left\{P^{\mathrm{SMR}}_{m,t,w}\right\}_\varphi$, $\left\{P^{\chi}_{t,w}\right\}_\varphi$, $\left\{R^{\varpi}_{t,w}\right\}_\varphi$

Algorithm 3 Typical days iteration

Input: Load data of the whole year, tolerance δ

Iteration step: $\Phi \leftarrow 1$
Cluster load data to get typical days.
Get the initial investment decisions $\left\{X_m, C^\beta\right\}_\Phi$ through **Algorithm 2**
repeat
  Based on load data, normalized PV output and PV capacity $\left\{C^P\right\}_\Phi$, cluster net load to get typical days.
  $\Phi \leftarrow \Phi + 1$
  Get the investment decisions $\left\{X_m, C^\beta\right\}_\Phi$ through **Algorithm 2**
until $\left|\left\{C^\beta\right\}_\Phi - \left\{C^\beta\right\}_{\Phi-1}\right| \leq \delta$

Output: Optimal investment decisions $\left\{X_m, C^\beta\right\}_\Phi$

D. Typical Days Adjustment

The inner iteration loop solves the frequency-constrained planning problem with the given typical days. The selection of typical days needs to consider the capacity decision-dependent PV generation to guarantee the representativeness of the typical daily net load profile. However, only the normalized PV output is available before planning. In this case, an outer iteration loop is proposed to iteratively use the difference between load and PV generation as net load for typical days selection. The outer iteration loop is given in **Algorithm 3**.

[1] $\beta \in \{\mathrm{PV}, \mathrm{B}, \mathrm{S}, \mathrm{SE}\}$, $\chi \in \{\mathrm{PV}, \mathrm{B}^+, \mathrm{B}^-, \mathrm{S}^+, \mathrm{S}^-\}$, $\varpi \in \{\mathrm{SMR}, \mathrm{PV}, \mathrm{B}\}$

TABLE II
RESOURCE PARAMETERS [18], [32], [28], [38]

Parameters	SMR	PV	BESS	SESS	H_2
Investment cost (k$-yr/MW)	1200	110	100	120	0.13
Operation cost ($/MWh)	24	–	–	–	–
Maximum capacity (MW)	10	10	2	6	10^4
Inertia constant	4.5	–	–	–	–
Minimum output	40%	0	0	0	–
Maximum reserve	10%	10%	20%	–	–

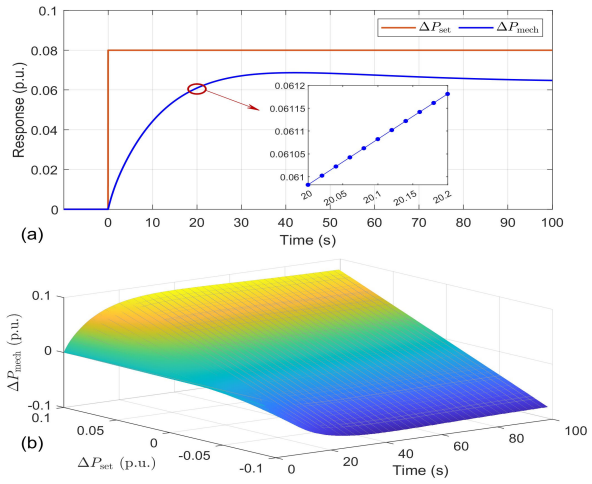

Fig. 9. (a) The dynamic trajectory of SMR's power output with a specific set point 0.08 p.u. (b) Dynamic trajectories of SMR's power output under different set points.

VI. CASE STUDIES

A. Experimental Setups

Case studies are conducted to verify the effectiveness of the proposed method. A net-zero energy system is planned to supply a remote standalone industrial/commercial load, for example, a data center in North China. The investment candidates include a set of identical SMRs (each modular rated at 0.5MW), PV, BESS, SESS, and H_2 storage. Load data and normalized available PV output of the entire year are estimated from historical data [18]. In our case, the load level is 10MW. All the generation units and storage devices are invested from scratch. The information of the resources is presented in Table. II. In terms of the frequency security requirements, the limits of RoCoF, steady-state deviation, and frequency nadir are set as: 0.5Hz/s, 0.5Hz, and 0.8Hz, respectively. The power imbalance P_{im} is considered as potential load variation, i.e., 5% of the load $L_{t,w}$ [30].

B. Dynamic Model Identification of SMR

1) Source Data: The dynamic model identification of SMR is based on the time-variant data of SMR's power output after a change in the set point from the EMS. Specifically, after the set point (input ΔP_{set}) of the SMR is changed, the dynamic response of the SMR's power output ΔP_{mech} is recorded. As shown in Fig. 4, the inputs for PINN training include

TABLE III
PINN CONFIGURATIONS

Parameter	Value
Optimizer	Adam
Activation function	Tanh
Hidden layers	5
Neurons per layer	10
Batch size	10,000
Training samples	400,000
Model parameters	b_2, b_1, b_0, a_2, a_1, a_0

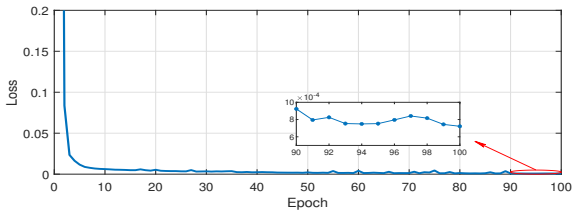

Fig. 10. PINN training process.

the set point ΔP_{set} and the time stamp τ. The output is the corresponding dynamic response ΔP_{mech}. In practice, the data can be recorded by the instrumentation systems of SMR. As SMR is still an emerging technology, we use simulation [13], [17] to obtain the dynamic response of SMR.

Since the dynamic response of SMR's power output ΔP_{mech} for frequency regulation is a small-scale deviation from the steady-state power output $P^{\text{SMR}}_{m,t,w}$, we normalize the response of ΔP_{mech} by the steady-state power output $P^{\text{SMR}}_{m,t,w}$. In this process, the input ΔP_{set} ranges from $\pm 10\%$ of the rated power, which is the upper limit for SMR's frequency reserve. Take an example of the set point as $\Delta P_{\text{set}} = 0.08$ p.u., the trajectory (time-variant data) of SMR's power output is shown in Fig. 9 (a). The trajectory of the dynamic response consists of 5,000 samples from $\tau = 0$ to $\tau = 100$s with the time step size 0.02s. Each sample includes the input (ΔP_{set}), the time stamp (τ), and the power output (ΔP_{mech}). We generate 100 trajectories through simulation by randomly selecting the set point ΔP_{set} from its range $[-0.1, 0.1]$ pu. The three-dimensional data include an arbitrary input and its time-variant output in the time interval $[0, 100]$ s, as shown in Fig. 9 (b). As a result, the entire dataset consists of 500, 000 samples. 80% of the samples (400, 000) are used for training and the other 20% samples (100, 000) are used for testing.

Generally, data cleaning needs to be conducted before the training process to address the possible missing values. Since the data we used is sourced from simulation, there are no missing values. In real applications, linear interpolation can be used to address the missing values [39].

2) PINN Configurations and Training Process: Based on the simulated data, PINN is adopted for the dynamic model identification of SMR, implemented using PyTorch. System order is determined as a balance between estimation accuracy and model complexity, which is selected from 1 to higher until the physics-informed Loss converges below 10^{-3}. Note that the Loss 10^{-3} is chosen by experiment results, which indicates

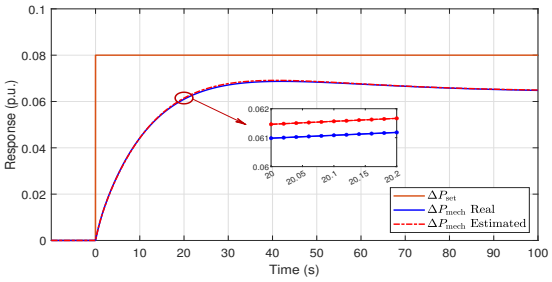

Fig. 11. Validation on the trajectory of the estimated model with a specific set point.

TABLE IV
PERFORMANCE OF THE ESTIMATED MODEL IN FITTING THE DATASET

Dataset	Training	Testing
MAPE	1.17%	1.21%

that the mean squared error (MSE) between the training dataset and the estimated output of PINN has converged below 10^{-3}. In this study, we find that a second-order model is enough to approximate the complex high-order model with satisfied accuracy. Our aim is to estimate the model parameters b_2, b_1, b_0, and a_2, a_1, a_0. Based on the methodology in Section III, the detailed PINN architecture is shown in Table III. The training process is shown in Fig. 10. From the results, the physics-informed loss function decreases with the number of epochs and converges below 10^{-3} after 100 epochs.

The PINN training is carried out on Intel (R) Xeon (R) W-3335 CPU @ 3.40GHz and NVIDIA GeForce RTX3080Ti with 188 GB installed RAM. The training time is influenced by the size of the network, the number of samples, and the batching strategy. In our PINN setting as shown in Table III, the training time required for each epoch is approximately 25 seconds and the whole training process takes 2382.08 seconds.

3) Model Validation: Through PINN training, the parameters of a second-order differential model are estimated, which is used to represent the dynamics of SMR in frequency regulation. The accuracy performance of the estimated model is validated concerning (1) training and testing datasets, and (2) frequency nadir approximation.

Accuracy on training and testing datasets: The time-variant output of the estimated model is compared with the output of the real SMR model recorded in the dataset to evaluate its performance. Take the input $\Delta P_{\text{set}} = 0.08$ p.u. as an example, the dynamic response of the estimated model tracks well with the real SMR model within the whole time horizon as shown in Fig. 11.

To quantitatively evaluate the accuracy performance of the estimated model on the dataset, the mean absolute percentage error (MAPE) is calculated as follows

$$\text{MAPE} = \frac{1}{N_c}\sum_{c=1}^{N_c}\left|\frac{\Delta P_{\text{mech},c} - \Delta\hat{P}_{\text{mech},c}}{\Delta P_{\text{mech},c}}\right|, \tag{29}$$

where N_c is the number of samples in the dataset. $\Delta P_{\text{mech},c}$ is the power output of the real SMR model recorded in sample c of the dataset. $\Delta\hat{P}_{\text{mech},c}$ is the power output derived from the estimated model with the same input ΔP_{set} and time stamp τ of sample c. Results in Table IV show that the MAPE for both training and testing datasets is below 2%, which indicates the high accuracy level of the estimated model in fitting the dataset of the real SMR model.

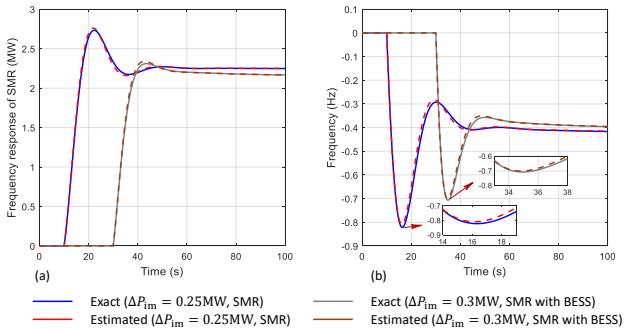

Fig. 12. Performance of the estimated SMR dynamic model in (a) frequency response and (b) frequency trajectory approximation under different scenarios.

TABLE V
PERFORMANCE OF THE ESTIMATED MODEL IN APPROXIMATING THE FREQUENCY NADIR

Scenarios	Case I	Case II	Case III	Case IV
MAPE	1.57%	0.92%	1.59%	0.94%

Accuracy on frequency nadir approximation: In our planning model, the estimated dynamic model of SMR is used to derive the frequency nadir, which is then integrated into the planning model as frequency security constraints. The performance of the estimated model obtained through PINN is evaluated in terms of frequency nadir estimation in this part. In case the estimated model is implemented for frequency regulation as shown in Fig. 7, the dynamic power output of SMR and system frequency trajectory approximation under different scenarios is presented in Fig. 12. From the results, the dynamic response of SMR's output and system frequency obtained from the estimated model fit well with the response of the real SMR model.

Similarly, MAPE is used to quantitatively evaluate the performance of the estimated model on frequency nadir approximation under different operation scenarios. Denote the frequency nadir (maximum deviation of frequency) as $\Delta f_{\text{nadir}} = |\Delta f|_{\max}$, MAPE is calculated as

$$\text{MAPE} = \frac{1}{N_e}\sum_{e=1}^{N_e}\left|\frac{\Delta f_{\text{nadir},e} - \Delta\hat{f}_{\text{nadir},e}}{\Delta f_{\text{nadir},e}}\right|, \tag{30}$$

where N_e is the number of validation experiments. $\Delta f_{\text{nadir},e}$ is the frequency nadir obtained through simulation of the real SMR model in experiment e. $\Delta\hat{f}_{\text{nadir},e}$ is the frequency nadir obtained through the estimated model in experiment e. We conduct the validation experiments based on our load level (10MW) under four different scenarios: 1) Case I: ΔP_{im} chosen as 5% load change, which ranges from -0.5MW to 0.5MW, SMR works alone to provide frequency response;

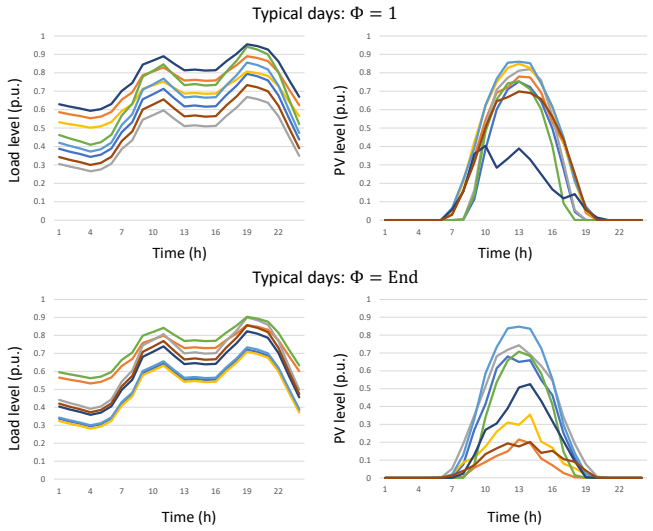

Fig. 13. Normalized load and PV output at different outer iteration steps.

2) Case II: ΔP_{im} chosen as 5% load change, SMR coordinates with the power electronics interfaced devices (BESS) to provide frequency response; 3) Case III: ΔP_{im} chosen as 15% load change, which ranges from -1.5MW to 1.5MW, SMR works alone to provide frequency response; 4) Case IV: ΔP_{im} chosen as 15% load change, SMR coordinates with the power electronics interfaced devices (BESS) to provide frequency response. For each case, we conduct 100 validation experiments by randomly selecting ΔP_{im} within the power imbalance range. From the results in Table V. The MAPE of the frequency nadir under different operation scenarios is below 2%. In particular, in Case II and Case IV when the SMR is coordinated with the power electronics interfaced devices (BESS), the MAPE of the frequency nadir estimation is below 1%. Therefore, the dynamic model obtained from PINN can be used to estimate the frequency nadir accurately during system operation.

C. Planning Results

1) Single Node System: At first, the capacity of PV is not determined and eight typical days are obtained through load clustering. After the investment capacity of PV is obtained at outer iteration step Φ, the difference between load and PV output is used as net load for typical days clustering at stage $\Phi+1$. In this process, the operation scenarios are better represented. The load and PV output at the first step and last step of each typical day are shown in Fig. 13, which indicates that through outer iteration, the typical days will be more representative. In the end, the investment capacity of the DERs converges within a difference of 0.05MW. The final investment decisions and costs at different outer iteration stages are presented in Table. VI. The results show that the investment decision changes with the invested PV capacity and the final investment capacity of PV converges to 8.47MW.

At the first step of the inner iteration process, the MILP planning model $\mathcal{P}_1$ is solved. The investment and operation decisions are used to evaluate the frequency nadir performance

TABLE VI
INVESTEMNT DECISIONS AND COSTS AT DIFFERENT OUTER ITERATION STAGES

Outer iteration stage		SMR	PV	BESS	SESS	Cost
$\Phi=1$	Cap (MW)	5.5	6.24	2	2.79	9.07
	Cost (M$)	7.73	0.69	0.2	0.45	
$\Phi=\text{End}$	Cap (MW)	5.5	8.47	2	2.44	9.33
	Cost (M$)	7.67	0.93	0.2	0.53	

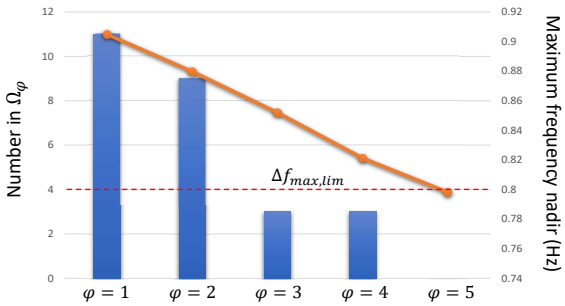

Fig. 14. The frequency nadir performance in the inner iteration process.

with Algorithm 1. Fig. 14 showcases the metrics describing the frequency nadir performance in the inner iteration process, where the number of time steps that violate the frequency nadir constraint (saved in Ω_φ) is counted. It can be seen that number is decreasing with the inner iteration step φ as the faster frequency responses from PV and BESS are enhanced. Meanwhile, the maximum value of the frequency nadir converges to the security range, i.e., less than 0.8Hz at the end of the inner iteration process. In the end, the frequency nadir constraint is satisfied at all the time steps.

For the time step in Ω_φ when the frequency nadir constraint is violated, the frequency dynamics at the first and last inner iteration step is presented in Fig. 15. The two linear frequency constraints, i.e., the maximum RoCoF constraint and the maximum steady-state frequency deviation constraint are inherently satisfied as they are integrated into the MILP planning model $\mathcal{P}_1$. For the non-linear frequency nadir constraint, through faster frequency response adjustment, the frequency nadir finally converges to the security range. In this process, more frequency reserves from BESS and PV are allocated.

The dispatched power outputs of DERs on certain typical days are shown in Fig. 16, where the intra-day and inter-day coordination of the invested resources are demonstrated. From the result in Fig. 16, SMRs operate at the nearly rated level. In typical day 3 when there is abundant PV generation, SMRs could adjust their outputs to promote the consumption of PV. BESS and SESS work as flexible resources to help satisfy the power balance under different load and PV generation scenarios. The results of typical day 1 and day 2 show the intra-day coordination of the resources, where the power output from SMRs and PV at lower load levels are charged in BESS and SESS devices and then discharged to supply for larger load levels at night. While the results of typical day 3 and day 4 show the inter-day coordination realized by SESS.

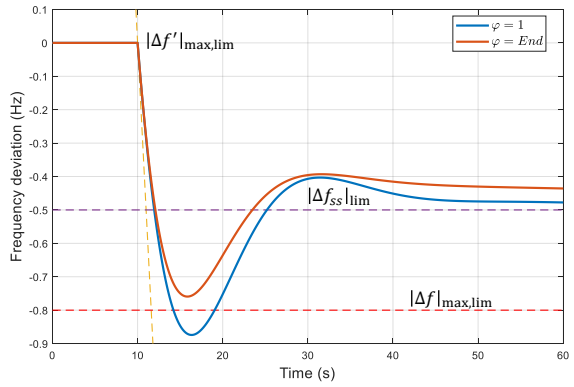

Fig. 15. Frequency response at the first and last inner iteration step.

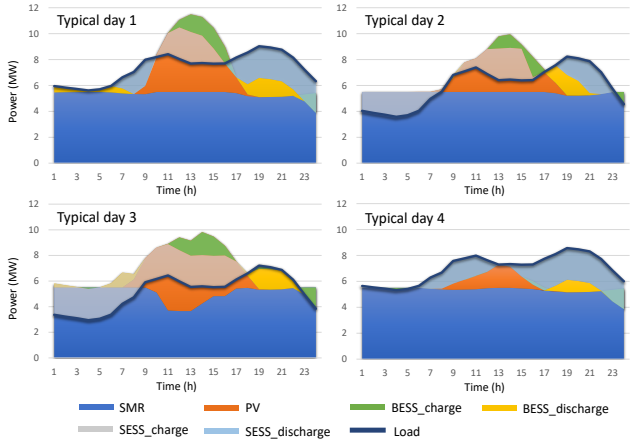

Fig. 16. The operation of different resources at certain representative days.

The excessive power output on day 3 is stored in SESS and discharged on day 4 when the generation level of PV is lower. In such a system configuration, there is no curtailment of PV, and energy efficiency is improved.

Since the planning horizon of 8760 hours is represented by several typical days through the clustering method, the number of representative days has a direct impact on the solution of the planning model. The planning results under different numbers of typical days are presented in Table. VII. With the increase of typical days, the operation scenarios in the whole year can be better represented, and the results will be more accurate. Table. VII shows that the investment capacity of SMR increases with the number of typical days since SMRs are more effective for balancing net-load fluctuations and providing frequency support.

From the results, the contributions of SMRs in the operation of net-zero energy systems are summarized: 1) SMRs provide base-load support for the system and the output can be adjusted in some operation scenarios for net load following. 2) The operation flexibility of BESS and SESS can be better utilized through SMR for intra-day and inter-day power balance. 3) SMRs provide both inertia and frequency regulation support for dynamic frequency security, which could improve the dynamic performance under a power imbalance contingency.

TABLE VII
RESULTS UNDER DIFFERENT NUMBER OF REPRESENTATIVE DAYS

Cluster Num	Cap (MW)				Cost (M$)
	SMR	PV	BESS	SESS	
4	5.5	7.31	2	1.97	9.26
8	5.5	8.47	2	2.44	9.33
12	6	4.90	2	2.32	9.48
16	6	6.53	2	2.32	9.62

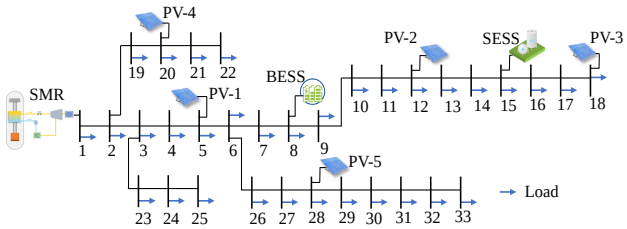

Fig. 17. Modified IEEE 33-bus network system.

2) Multi-node System: To illustrate the scalability of the proposed method, case studies based on a multi-node (bus) system are conducted. We apply the proposed model to a modified IEEE 33-bus low-voltage network as shown in Fig. 17. The investment candidates include SMR modules (Bus 1), five PV plants (Bus 5, 12, 18, 20, 28), BESS (Bus 8), and SESS (Bus 15). The system load is distributed to all the buses. The system parameters are the same as in Table II. Different from the single-node system, the supply-demand balance needs to be satisfied at each node of the system. Meanwhile, the power flow model and distribution line capacity constraints also need to be satisfied. The additional network associated constraints are represented the same as [28]. The investment decisions include the capacity of the generation units at each bus.

The planning results under 12 typical days are shown in Table VIII. Compared with the results of the single-node system in Table VII, the invested capacities of SMR, BESS, and SESS are consistent while more PV generation is invested. Moreover, the distribution of PV's investment is impacted by the network structure and the line flow constraints. Since SMR in Bus 1 could provide sufficient generation for the system, there are no PV investments in Bus 5 and Bus 20. More PV generation is needed in Bus 12, Bus 18, and Bus 28 due to the limited capacity of the distribution line from Bus 9 to Bus 10 and the distribution line from Bus 6 to Bus 26. For SESS, the capacity of the H_2 storage is also increased to help accommodate the PV generation in Bus 12 and Bus 18.

Additionally, the computational time for different numbers of typical days of the planning model with the network model is provided in Table IX. All case studies have been performed on Intel (R) Xeon (R) W-3335 CPU @ 3.40GHz and NVIDIA GeForce RTX3080Ti. Intuitively, the computational time increases with the number of typical days since more decision variables and constraints are introduced. The increase in the computational time between the MILP planning problem solution and the three-stage solution method indicates that the

TABLE VIII
PLANNING RESULTS WITH NETWORK MODEL INTEGRATED

	SMR	PV-2	PV-3	PV-5	BESS	SESS
Cap (MW)	6	2.66	1.22	2.65	2	2.33
Cost (M$)	8.27	0.29	0.13	0.29	0.2	0.43

TABLE IX
COMPUTATIONAL TIME OF THE MULTI-NODE SYSTEM UNDER DIFFERENT TYPICAL DAYS

No. of typical days	4	8	12	16
Computation time (s) of MILP planning	576.34	650.81	777.98	815.15
Computation time (s) of three-stage strategy	1762.7	2857.24	3983.17	4775.18

proposed method could get a feasible solution after a few iterations efficiently.

D. Comparative Analysis

1) Ablation Analysis on Frequency Reserve: The proposed model is compared with other two cases to verify its effectiveness:

Case1: Microgrid planning with no frequency security constraints.

Case2: Microgrid planning with fixed frequency reserve (10% of rated power output) for dynamic frequency security.

Case3 (Our Method): Microgrid planning with variable frequency reserve.

The final planning decisions under the three cases are presented in Table X. Compared with the results of Case1 and Case2, the proposed method can guarantee the frequency security constraints with less increased cost (1%). The operation flexibility from SMR and energy storage devices is better utilized and coordinated to satisfy the steady operation constraints and dynamic frequency security constraints.

2) Comparison with Coal-fired Generator Based Systems: The proposed SMR-renewable energy system is compared with other system configurations to illustrate its feasibility in net-zero design. The planning model is actually a multi-objective optimization problem with economic, low-carbon, and security considerations. From an environmental perspective, renewable energy resources could be coordinated with energy storage systems as a net-zero solution. However, these resources are all connected to the system through power electronics interfaces, which challenges frequency security due to the lack of inertia [40]. Thus, such a system configuration is infeasible for security requirements. Traditional coal-fired thermal generators could be used to help satisfy frequency security requirements. However, there will be inherent carbon emissions. With the low-carbon development of energy systems, there will be additional environmental costs for carbon emissions, e.g. carbon tax, or carbon capture costs [41]. Although SMR is currently costly, it can be economically competitive with the requirement of low carbon emission. To

TABLE X
RESULTS OF DIFFERENT PLANNING MODELS

Cases		SMR	PV	BESS	SESS	Cost
Case1	Cap (MW)	5.5	7.37	1.84	2.19	9.24
	Cost (M$)	7.69	0.81	0.18	0.56	
Case2	Cap (MW)	6	9.17	2	2.25	10.06
	Cost (M$)	8.28	1.01	0.2	0.57	
Case3	Cap (MW)	5.5	8.47	2	2.44	9.33
	Cost (M$)	7.67	0.93	0.2	0.53	

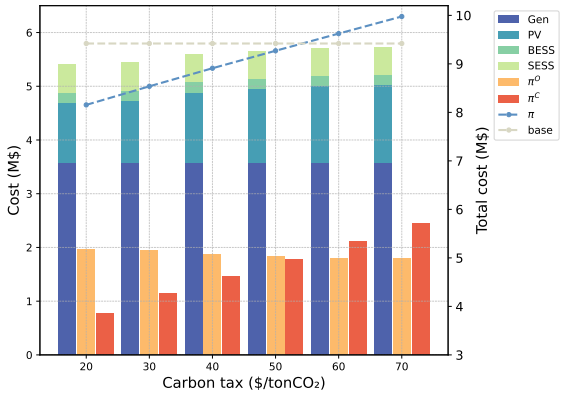

Fig. 18. Cost of coal-fired thermal generator based system configuration under different values of carbon tax.

illustrate the economic feasibility of SMRs compared with coal-fired thermal generators under low carbon development, we conduct a sensitivity analysis on the impact of carbon tax [42].

The system configuration of coal-fired generators is similar to Fig. 1 where SMRs are replaced by coal-fired generators. The overall cost π includes investment cost π^I, operation cost π^O, and the additional environment cost π^C associated with carbon emission as

$$\pi^C = \iota \cdot \vartheta \sum_{w=1}^{W} \sum_{t=1}^{T} \psi_w P_{t,w}^{\text{Coal}}, \tag{31}$$

where ι is the carbon emission intensity (tonCO_2/MWh). ϑ represents the carbon tax (\$/tonCO_2). $P_{t,w}^{\text{Coal}}$ is the power output of coal-fired generators. The objective function of the planning model is reformulated as

$$\min \ \pi = \pi^I + \pi^O + \pi^C. \tag{32}$$

The cost parameters and constraints of coal-fired generators associated with planning and operations are from [28]. The values of carbon emission intensity and carbon tax are sourced from [42]. Currently, the carbon tax ranges from 20 \$/tonCO_2 to 70 \$/tonCO_2 [41] in different countries. With 12 typical days chosen as the planning scenarios, the planning results are shown in Fig. 18. It can be seen that the invested capacity of coal-fired generators (Gen) remains the same with the increase of the carbon tax, which is constrained by the inertia

requirement for frequency security. There is a decrease in the total generation of coal-fired generators, which is posed by the increased carbon tax. In this case, the operating hours and utilization efficiency of coal-fired generators are reduced. PV's investment capacity increases with the carbon tax as PV is a clean energy source that could compensate for the reduced supply from coal-fired generators.

The overall costs of coal-fired generators based system and our proposed SMR-based system configurations are also shown in Fig. 18. As SMR is a clean energy source, the environmental cost π^C of our proposed SMR-renewable energy system is zero and the overall cost remains unchanged with carbon tax. In this case, the overall cost of the planned SMR-renewable system in Table VII is represented as the base value. For coal-fired generators integrated systems, the overall cost increases with the carbon tax. It can be seen that when the carbon tax is less than 60 \$/tonCO_2, it is more economical to select the coal-fired generators as the base-load support for the standalone energy system. However, with the decarbonization development of energy systems, the carbon tax will be higher. In the cases when the carbon tax is equal or higher than 60 \$/tonCO_2, SMRs become more economically competitive. In addition, the costs of SMRs will decrease with the technical development [11], which will enhance the feasibility of SMRs for net-zero energy systems.

E. Sensitivity Analysis

The system designed in this work is able to sustain frequency security under a sudden power imbalance contingency. As shown in (18)-(25), the frequency security constraints are determined by the predefined power imbalance ΔP_{im}, which would impact the requirements on frequency reserve of different resources and thus result in different system configurations. Apart from the 5% load change considered in the previous cases, we conduct sensitivity analysis on different power imbalance scenarios in this part. Two different cases are considered:

Case1: Power imbalance ΔP_{im} from different levels of load uncertainty;

Case2: Power imbalance ΔP_{im} from different levels of load and PV uncertainty.

Since BESS works as a flexible resource with faster frequency response, it can be used to provide both virtual inertia and frequency regulation support. In particular, more faster frequency response from BESS is needed to satisfy frequency nadir constraints. To guarantee the feasibility of the planning model under larger power imbalance scenarios, we enlarge the capacity limit of BESS to 3MW in the cases of this part. The results of the frequency reserve requirements in the worst scenario (maximum power imbalance ΔP_{im}) are shown in Fig. 19. The planning results under different scenarios are shown in Table XI. From both cases, it can be seen that SMRs' maximum frequency reserve (10% of rated power) is fully activated in the worst scenario under different uncertainty levels. The required frequency reserve from BESS increases with the uncertainty level. When the flexible resource BESS is sufficient to provide frequency regulation service (Case1), there are fewer requirements on frequency reserve from PV. When the power imbalance is larger (Case2), PV's frequency reserve is also activated to help sustain frequency security.

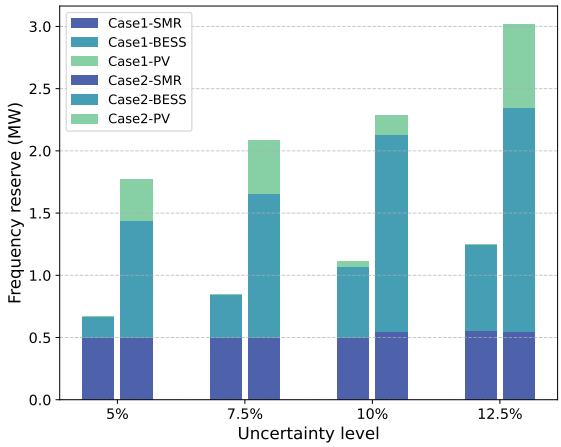

Fig. 19. Frequency reserve of DERs in the worst power imbalance scenario under different uncertainty levels.

TABLE XI
PLANNING RESULTS UNDER DIFFERENT POWER IMBALANCE CASES WITH DIFFERENT UNCERTAINTY LEVELS

Uncertainty level		SMR	PV	BESS	SESS
5%	Case1 (MW)	5	10	3	3.53
	Case2 (MW)	5	10	3	3.61
7.5%	Case1 (MW)	5	10	3	3.53
	Case2 (MW)	5	10	3	3.73
10%	Case1 (MW)	5	10	3	3.53
	Case2 (MW)	5.5	7.55	2.85	2.84
12.5%	Case1 (MW)	5.5	7.42	3	3.21
	Case2 (MW)	5.5	7.74	3	3.21

From the planning results, it can be seen that the planning results from 5% to 10% load uncertainty (Case1) remain unchanged. The reason is that the frequency reserve from BESS is sufficient and the reserve could be optimized to guarantee frequency security under different scenarios. With the increase in uncertainty level, there will be more investment in SMRs, which indicates that BESS's flexibility could not sustain a larger system imbalance alone and more inertia and frequency regulation support from the SMR is needed. On the contrary, there is a decrease in PV's invested capacity since the added SMRs could help supply the demand, and less PV generation is needed.

VII. CONCLUSIONS

This paper proposes a net-zero planning approach for standalone energy systems with SMRs. which could provide a feasible solution to the decarbonization of energy systems. Both steady-state operation constraints and dynamic frequency security constraints are considered. Specifically, the dynamic response of SMR is identified as a transfer function model through a data-driven method. The dynamic responses of

different resources are aggregated to derive the frequency security constraints and introduced to the planning model. Furthermore, to address the nonlinearity caused by frequency nadir constraint, a heuristic solution method is proposed with fast frequency reserve adjustment. The results suggest that: 1) SMR could work as low-carbon flexible resources to support the development of net-zero energy systems. 2) SMR could help to provide inertia and frequency regulation service to ensure the reliability of operation under a sudden contingency.

REFERENCES

[1] X. Wu, B. Cao, B. Liu, and X. Wang, "A planning model of standalone hydrogenbased carbon-free microgrid through convex relaxation," *IEEE Transactions on Smart Grid*, pp. 1–1, 2022.

[2] R. O'Connell, A. Phadke, M. O'Boyle, C. T. Clack, P. Denholm, and B. Ernst, "Carbon-free energy: how much, how soon?" *IEEE Power and Energy Magazine*, vol. 19, no. 6, pp. 67–76, 2021.

[3] D. Michaelson and J. Jiang, "Integration of small modular reactors into renewable energy-based standalone microgrids: An energy management perspective," *IEEE Power and Energy Magazine*, vol. 20, no. 2, pp. 57–63, 2022.

[4] H. Ahmadi and H. Ghasemi, "Security-constrained unit commitment with linearized system frequency limit constraints," *IEEE Trans. Power Systems*, vol. 29, no. 4, pp. 1536–1545, 2014.

[5] X. Shen, X. Li, J. Yuan, and Y. Jin, "A hydrogen-based zero-carbon microgrid demonstration in renewable-rich remote areas: System design and economic feasibility," *Applied Energy*, vol. 326, p. 120039, 2022.

[6] L. F. Cabeza, C. Sole, A. Castell, E. Oro, and A. Gil, "Review of solar thermal storage techniques and associated heat transfer technologies," *Proceedings of the IEEE*, vol. 100, no. 2, pp. 525–538, 2011.

[7] M. N. S. K. Shabbir, M. S. A. Chowdhury, and X. Liang, "A guideline of feasibility analysis and design for concentrated solar power plants," *Canadian Journal of Electrical and Computer Engineering*, vol. 41, no. 4, pp. 203–217, 2018.

[8] H. Subki, "Advances in small modular reactor technology developments," 2020.

[9] T. R. McJunkin and J. T. Reilly, "Net-zero carbon microgrids," Idaho National Lab.(INL), Idaho Falls, ID (United States), Tech. Rep., 2021.

[10] B. Poudel, T. R. McJunkin, N. Kang, J. T. Reilly, and M. Stadler, "Small reactors in microgrids: Technoeconomic analysis," Idaho National Lab.(INL), Idaho Falls, ID (United States), Tech. Rep., 2022.

[11] B. Poudel, T. R. McJunkin, N. Kang, J. T. Reilly, R. Guerrero, and M. Stadler, "Small reactors in microgrids: Technology modeling and selection," Idaho National Laboratory (INL), Idaho Falls, ID (United States), Tech. Rep., 2023.

[12] N. R. Canada. (2018) A call to action: a canadian roadmap for small modular reactors. Accessed on September 17, 2023. [Online]. Available: https://smrroadmap.ca/

[13] B. Poudel, K. Joshi, and R. Gokaraju, "A dynamic model of small modular reactor based nuclear plant for power system studies," *IEEE Trans. Energy Conversion*, vol. 35, no. 2, pp. 977–985, 2019.

[14] A. Sabir, D. Michaelson, and J. Jiang, "Load-frequency control with multimodule small modular reactor configuration: Modeling and dynamic analysis," *IEEE Trans. Nuclear Science*, vol. 68, no. 7, pp. 1367–1380, 2021.

[15] D. Ingersoll, C. Colbert, Z. Houghton, R. Snuggerud, J. Gaston, and M. Empey, "Can nuclear power and renewables be friends?" in *Proceedings of ICAPP*, vol. 2015, 2015.

[16] B. Poudel and R. Gokaraju, "Optimal operation of smr-res hybrid energy system for electricity & district heating," *IEEE Trans. Energy Conversion*, vol. 36, no. 4, pp. 3146–3155, 2021.

[17] H. A. Gabbar and O. L. A. Esteves, "Real-time simulation of a small modular reactor in-the-loop within nuclear-renewable hybrid energy systems," *Energies*, vol. 15, no. 18, p. 6588, 2022.

[18] H. Li, Y. Qiao, Z. Lu, B. Zhang, and F. Teng, "Frequency-constrained stochastic planning towards a high renewable target considering frequency response support from wind power," *IEEE Trans. Power Systems*, vol. 36, no. 5, pp. 4632–4644, 2021.

[19] Z. Zhang, E. Du, F. Teng, N. Zhang, and C. Kang, "Modeling frequency dynamics in unit commitment with a high share of renewable energy," *IEEE Trans. Power Systems*, vol. 35, no. 6, pp. 4383–4395, 2020.

[20] M. Paturet, U. Markovic, S. Delikaraoglou, E. Vrettos, P. Aristidou, and G. Hug, "Stochastic unit commitment in low-inertia grids," *IEEE Trans. Power Systems*, vol. 35, no. 5, pp. 3448–3458, 2020.

[21] Y. Zhang, H. Cui, J. Liu, F. Qiu, T. Hong, R. Yao, and F. Li, "Encoding frequency constraints in preventive unit commitment using deep learning with region-of-interest active sampling," *IEEE Trans. Power Systems*, vol. 37, no. 3, pp. 1942–1955, 2021.

[22] Z. Chu, N. Zhang, and F. Teng, "Frequency-constrained resilient scheduling of microgrid: A distributionally robust approach," *IEEE Trans. Smart Grid*, vol. 12, no. 6, pp. 4914–4925, 2021.

[23] A. M. Nakiganda, S. Dehghan, U. Markovic, G. Hug, and P. Aristidou, "A stochastic-robust approach for resilient microgrid investment planning under static and transient islanding security constraints," *IEEE Trans. Smart Grid*, vol. 13, no. 3, pp. 1774–1788, 2022.

[24] B. Huang and J. Wang, "Applications of physics-informed neural networks in power systems-a review," *IEEE Trans. Power Systems*, 2022.

[25] M. Zhang, Q. Xu, and X. Wang, "Physics-informed neural network based online impedance identification of voltage source converters," *IEEE Trans. Industrial Electronics*, vol. 70, no. 4, pp. 3717–3728, 2022.

[26] G. S. Misyris, A. Venzke, and S. Chatzivasileiadis, "Physics-informed neural networks for power systems," in *2020 IEEE Power & Energy Society General Meeting (PESGM)*. IEEE, 2020, pp. 1–5.

[27] D. P. Kingma and J. Ba, "Adam: A method for stochastic optimization," *arXiv preprint arXiv:1412.6980*, 2014.

[28] E. Du, N. Zhang, B.-M. Hodge, Q. Wang, C. Kang, B. Kroposki, and Q. Xia, "The role of concentrating solar power toward high renewable energy penetrated power systems," *IEEE Trans. Power Systems*, vol. 33, no. 6, pp. 6630–6641, 2018.

[29] B. Mignacca and G. Locatelli, "Economics and finance of small modular reactors: A systematic review and research agenda," *Renewable and Sustainable Energy Reviews*, vol. 118, p. 109519, 2020.

[30] T. Baškarad, I. Kuzle, and N. Holjevac, "Photovoltaic system power reserve determination using parabolic approximation of frequency response," *IEEE Trans. Smart Grid*, vol. 12, no. 4, pp. 3175–3184, 2021.

[31] Y. Wu, G. J. Lim, and J. Shi, "Stability-constrained microgrid operation scheduling incorporating frequency control reserve," *IEEE Transactions on Smart Grid*, vol. 11, no. 2, pp. 1007–1017, 2019.

[32] W. Mark, Z. Ali, T. Don, B. Jacopo, and S. Koroush, "Techno-economic assessment for generation iii+ small modular reactor deployments in the pacific northwest," 2021.

[33] Y. Ma, Z. Hu, and Y. Song, "Hour-ahead optimization strategy for shared energy storage of renewable energy power stations to provide frequency regulation service," *IEEE Trans. Sustainable Energy*, vol. 13, no. 4, pp. 2331–2342, 2022.

[34] L. Kotzur, P. Markewitz, M. Robinius, and D. Stolten, "Time series aggregation for energy system design: Modeling seasonal storage," *Applied Energy*, vol. 213, pp. 123–135, 2018.

[35] J. Tan, Q. Wu, and X. Zhang, "Optimal planning of integrated electricity and heat system considering seasonal and short-term thermal energy storage," *IEEE Trans. Smart Grid*, 2022.

[36] Y. Yuan, Y. Zhang, J. Wang, Z. Liu, and Z. Chen, "Enhanced frequency-constrained unit commitment considering variable-droop frequency control from converter-based generator," *IEEE Transactions on Power Systems*, vol. 38, no. 2, pp. 1094–1110, 2022.

[37] Z. Chu, U. Markovic, G. Hug, and F. Teng, "Towards optimal system scheduling with synthetic inertia provision from wind turbines," *IEEE Trans. Power Systems*, vol. 35, no. 5, pp. 4056–4066, 2020.

[38] P. Gabrielli, M. Gazzani, E. Martelli, and M. Mazzotti, "Optimal design of multi-energy systems with seasonal storage," *Applied Energy*, vol. 219, pp. 408–424, 2018.

[39] K. Usman and M. Ramdhani, "Comparison of classical interpolation methods and compressive sensing for missing data reconstruction," in *2019 IEEE International Conference on Signals and Systems (ICSigSys)*. IEEE, 2019, pp. 29–33.

[40] B. Kroposki, B. Johnson, Y. Zhang, V. Gevorgian, P. Denholm, B.-M. Hodge, and B. Hannegan, "Achieving a 100% renewable grid: Operating electric power systems with extremely high levels of variable renewable energy," *IEEE Power and Energy Magazine*, vol. 15, no. 2, pp. 61–73, 2017.

[41] M. Santikarn, A. N. Churie Kallhauge, M. O. Bozcaga, L. Sattler, M. S. Mccormick, A. Ferran Torres, D. Conway, L. Mongendre, C. Inclan, S. Mikolajczyk *et al.*, "State and trends of carbon pricing 2021," 2021.

[42] Y. Cheng, N. Zhang, B. Zhang, C. Kang, W. Xi, and M. Feng, "Low-carbon operation of multiple energy systems based on energy-carbon integrated prices," *IEEE Transactions on Smart Grid*, vol. 11, no. 2, pp. 1307–1318, 2019.

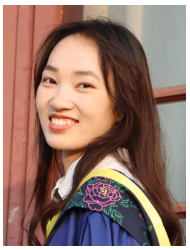

Mingyu Huang received her B.S. degree in automation in 2019 and her M.S. degree in control science and engineering in 2022, both from Wuhan University, Wuhan, China. She is currently pursuing her Ph.D. degree in the Department of Electrical and Electronic Engineering at the University of Hong Kong. Her research interests include dynamic virtual power plants and ancillary services.

Xueyuan Cui received the B.E. and M.S. degrees from Zhejiang University, Hangzhou, China, in June 2019 and March 2022, respectively, both in electrical engineering. He is currently a Ph.D. student with the Department of Electrical and Electronic Engineering, The University of Hong Kong. His research interests include power system operation and network balancing technologies.

Ning Zhang (S'10, M'12, SM'18) received both B.S. and Ph.D. from the Electrical Engineering Department of Tsinghua University in China in 2007 and 2012, respectively.

He is now Tenured Associate Professor at the same university. His research interests include renewable energy, and low carbon power system planning and operation, multi-energy systems integration.

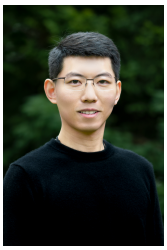

Mengshuo Jia (S'18 M'21) received the B.E. degree in electrical engineering from North China Electric Power University in 2016, and the Ph.D. degree in electrical engineering from Tsinghua University in 2021. From 2021 to 2023, He was a Postdoctoral Researcher with the Department of Information Technology and Electrical Engineering, ETH Zürich, where he is now a Senior Scientist and a PI funded by the Swiss National Science Foundation (SNSF). He is also an Associate Editor for IEEE Systems Journal and the IET Renewable Power Generation. His research interests include data-driven modeling and planning.

Yi Wang (Member, IEEE) received the B.S. degree from Huazhong University of Science and Technology in June 2014, and the Ph.D. degree from Tsinghua University in January 2019. He was a visiting student with the University of Washington from March 2017 to April 2018. He served as a Postdoctoral Researcher in the Power Systems Laboratory, ETH Zurich from February 2019 to August 2021.

He is currently an Assistant Professor with the Department of Electrical and Electronic Engineering, The University of Hong Kong. His research interests include data analytics in smart grids, energy forecasting, multi-energy systems, Internet-of-things, cyber-physical-social energy systems.